National Aeronautics and Space Administration

Orbital Debris Quarterly News

Volume 25, Issue 4
December 2021

Inside...

A publication of the NASA Orbital Debris Program Office (ODPO)

Accidental Collision of YunHai 1-02

The 18th Space Control Squadron (18 SPCS) of the U.S. Space Force has identified the breakup of China's YunHai 1-02 meteorological spacecraft (International Designator 2019-063A, Catalog number 44547) on 18 March 2021 (ODQN, vol. 25, issue 2, p.1) to be an accidental collision with a tracked object. That object (International Designator 1996-051Q, Catalog number 48078) was a small, mission-related debris associated with the SL-16 launch vehicle for the deployment of Cosmos 2333 in 1996. The YunHai 1-02 breakup marked the fifth confirmed accidental collision between two cataloged objects. A total of 37 fragments from the collision have been cataloged by the 18 SPCS and as of 1 October 2021, 4 of them have decayed. ♦

Five confirmed accidental collisions between cataloged objects

Event Date	Object 1 - (Int'l Designator, Catalog Number)	Object 2 - (Int'l Designator, Catalog Number)	Number of Cataloged Fragments
23 Dec 1991	Cosmos 1934 (1988-023A, 18985)	Mission-related debris (1977-062C, 13475)	3
24 Jul 1996	CERISE* (1995-033B, 23606)	Fragmentation debris (1986-019RF, 18208)	2
17 Jan 2005	DMSP 5B F5 upper stage (1974-015B, 7219)	Fragmentation debris (1999-057CV, 26207)	7
10 Feb 2009	Iridium 33* (1997-051C, 24946)	Cosmos 2251 (1993-036A, 22675)	2370
18 Mar 2021	YunHai 1-02* (2019-063A, 44547)	Mission-related debris (1996-051Q, 48078)	37

**Operational at the time of collision*

Updated NASA Technical Standard for Limiting Orbital Debris

The NASA Technical Standard (NS) 8719.14 revision C, Process for Limiting Orbital Debris, was signed by NASA's Chief of Safety and Mission Assurance, Mr. W. Russ DeLoach, on 5 November 2021. This revision focuses on changes and updates incorporated into the 2019 U.S. Government Orbital Debris Mitigation Standard Practices (ODMSP), which include improvements to the original 2001 ODMSP objectives, as well as clarification and additional standard practices for special classes of space missions (ODQN, vol. 24, issue 1, pp.1 and pp. 4-8).

The NASA Orbital Debris Program Office also has updated the NASA Debris Assessment Software (DAS) to version 3.2 to assist projects for mission compliance assessments with the requirements, old and new, in the revised standard. NS 8719.14 is available at https://standards.nasa.gov/standard/nasa/nasa-std-871914. DAS 3.2 will be located in the NASA Software Catalog and can be requested via the NASA Technology Transfer Program (https://software.nasa.gov/software/MSC-26690-1). ♦

PROJECT REVIEW

Experimental Hypervelocity Impacts of Non-Spherical Projectiles on Whipple Shields

J. MILLER, B. DAVIS, R. MCCANDLESS, A. DELGADO, D. HENDERSON, A. PARDO, D. RODRIGUEZ, AND M. SANDY

The DebriSat hypervelocity impact experiment performed at the Arnold Engineering Development Center in April 2014 [1] was conducted to update the catastrophic break-up models for modern satellites [2]. To this end, the DebriSat body was built with many modern materials, including structural panels of carbon-fiber reinforced polymer (CFRP), wires, and representative metallic storage tanks. Fragments from the DebriSat laboratory impact experiment were captured by and extracted from porous catcher panels for characterization [3]. To date, a key observation is that CFRP fragments represent a large fraction of the collected debris and that these fragments tend to be thin, "flake-like" structures or long, "needle-like" structures; whereas debris with nearly equal dimensions is less prevalent [4]. Additionally, high-density metals such as steel and copper are also prevalent and of special concern, considering their ability to compromise shields. As current ballistic-limit models for shields are based upon spherical impacting particles [5], the DebriSat experiment has a missing component in the current approach to ballistic modeling that must be considered in defining the protection capability of a shield. To improve risk assessments of spacecraft reliability and survivability, refined, broad-ranging, non-spherical, ballistic-limit equations are needed to address the DebriSat findings.

While numerous shield types are currently in use for impact mitigation from orbital debris and meteoroids, the most common shield in use is the double-wall shield commonly known as a Whipple shield [6]. This shield achieves a high level of ballistic performance for minimal weight because the stresses induced in a projectile during impact are far above the stresses the solid particle can withstand, resulting in a break-up of the particle. In the Whipple shield approach, an empty volume between the two walls of the shield creates an empty space for the debris cloud to expand that results in a distributed impact on the second shield-wall; however, even with the increased performance of this design, the shield-wall reaches a limiting size, called the ballistic limit [7].

To guide numerical simulations of this highly prevalent shield, a series of all-metal, Whipple shield research experiments have been performed to validate models. Previous ODQN articles described the development of a numerical simulation model (ODQN, vol. 22, issue 4, November 2018, pp. 2-4) and validation data (ODQN, vol. 24, issue 3, August 2020, pp. 5-8) for a specific shield system with an overlying blanket that is representative of an International Space Station shield; however, for a more fundamental understanding of the Whipple shield performance, the material configuration, shown in Figure 1 has recently been considered. This shield is nearly identical to those mentioned above, but it is missing the overlying blanket. By removing the overlying blanket, the influence of the metallic elements' constitutive properties is isolated; however, this change also reduced overall shield performance requiring the development of new facility capabilities for smaller projectiles.

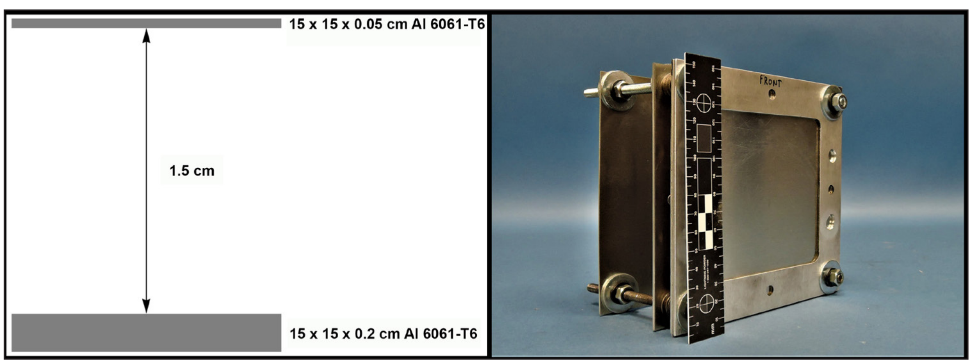

Figure 1. The experimental configuration for the shape effect research including the diagram of the Whipple shield target (left) and image of a representative target (right).

The Hypervelocity Impact Technology group (HVIT) at the NASA Johnson Space Center and the Remote Hypervelocity Test Laboratory (RHTL) at the NASA White Sands Test Facility in Las Cruces, New Mexico teamed up to acquire representative impacts of right-circular-cylinder projectiles using the 0.17-caliber range at RHTL. Right-circular-cylinder projectiles have been accelerated using a separable sabot with the range's two-stage, light-gas-gun to about 7 km/s into the shield. Moving to this range shortened the working distance for the cameras enabling higher magnification settings that are needed for tracking these smaller projectiles.

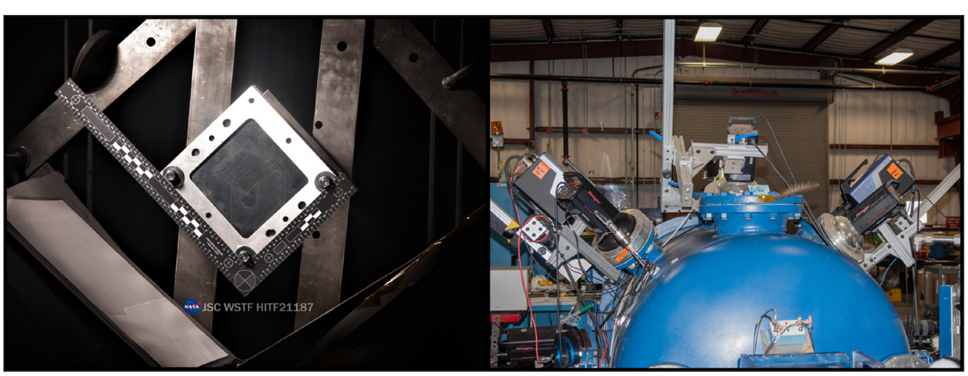

Figure 2. The research article is placed in a stationary target mount that holds the target during the shot and provides a back screen (left). Illumination sources and high-speed cameras are mounted outside the 0.17-caliber target tank (right). The experimental setup records projectile motion at 5 million frames per second and at a spatial resolution of 10 micrometers.

The Whipple shield targets are used within a specially designed target mount, shown in Figure 2, to maintain the proper orientation of the targets with respect to the range. The target mount directly interfaces with the target chamber and holds the primary

continued on page 3

Whipple Shield HVITs

continued from page 2

target and alignment tool for setting up and calibrating two frame-synchronized, high-speed cameras outside the target tank, also shown in Figure 2, between each shot. This dual frame approach allows the rapid and repeatable change out of targets between successive shots without altering the alignment of the projectile integrity and orientation cameras outside of the target chamber. It also allows for calibration of projectile orientation to support simulations and modeling development.

While all projectiles are accelerated with their central axis pointed toward the target, the release from the carrying sabot and the flight within the target chamber result in the potential of a non-prescribed rotation of the projectile. Prior to firing the shots, the cameras, located 45° down from the top of the target chamber, are focused on an alignment fixture that is placed immediately in front of the target. The alignment fixture provides a reference to adjust the cameras so that they are orthogonal, and the fixture has features for focus adjustment as well as spatial fiducials for scaling the camera images at the expected position of the projectile in flight. From these two orthogonal views, angles between the cylinder's axis and the velocity vector can be measured for each view. These orthogonal rotation angles can then be used to calculate the true pitch-angle between the cylinder axis and velocity vector, which is not necessarily in either view.

As mentioned early on, an objective of this research is to understand shield performance based on projectile geometry and for both low- and high-density projectiles. The low-density projectiles have been derived from both an axially extruded fiber system with a rod-stock form that has a high performance Bisphenol A epoxy resin binder [8], and plane-woven, 1/32 inch- and 1/16 inch-thick, sheet-stock of ultra-strength, lightweight carbon-fiber [9]. For the high-density metallic projectiles, both C11000 copper and T-304L stainless-steel round bar have been used. All projectile dimensions are characterized to a 25 µm resolution using a VHX-5000 series digital microscope manufactured by KEYENCE Corporation of America.

For the low-density, "needle-like" geometry, a characteristic image of the CFRP projectile from HITF21187 is shown in Figure 3. In shot HITF21187, a 2.941 mm long by 1.029 mm diameter CFRP rod has been launched at 7.05 km/s normal to the surface of the target. During its flight, the CFRP rod rotated to a pitch of 30.2° during the sabot separation. In Figure 3, the debris cloud evolution within the Whipple shield is shown at 400 ns intervals with time progressing from the top left to the bottom right. In the last frame shown, the debris cloud shock-wave compression begins to superheat the debris-cloud gases and saturates the camera view.

The resultant entrance hole into the shield and the front surface of the arresting rear wall is shown in Figure 4. The shield remained intact for

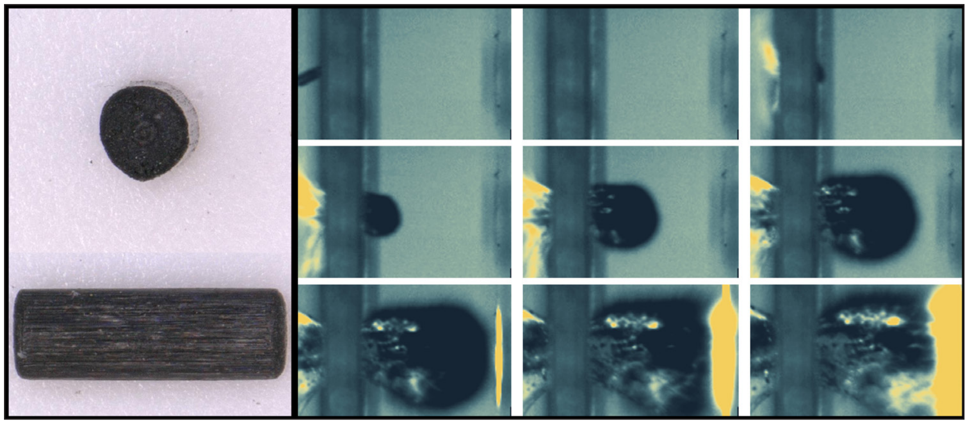

Figure 3. Images from HITF21187, which is the impact of a 2.941 mm long by 1.029 mm diameter CFRP projectile at 7.05 km/s (left). In-situ debris cloud images have been collected from just prior to the initial impact of the projectile and to interaction with the rear wall of the Whipple shield. The interframe interval shown is at 400 nanoseconds (right).

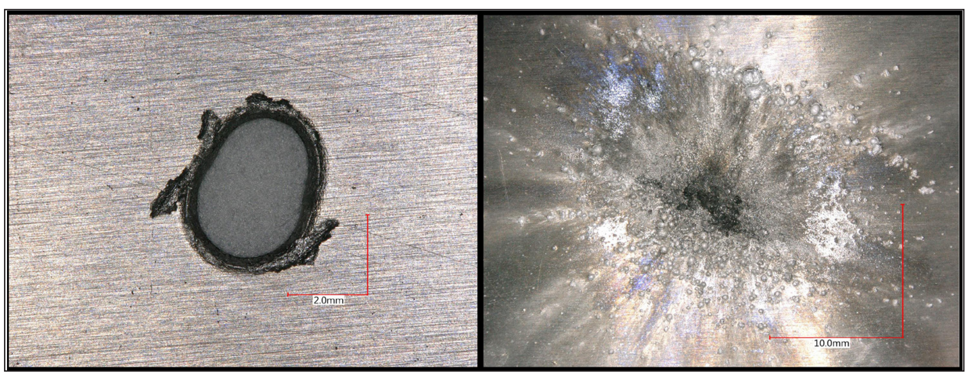

Figure 4. The results of HITF21187 are shown for the entrance hole into the shield (left) and for the crater field from the debris cloud in the rear wall (right). The shield remained intact from the impact.

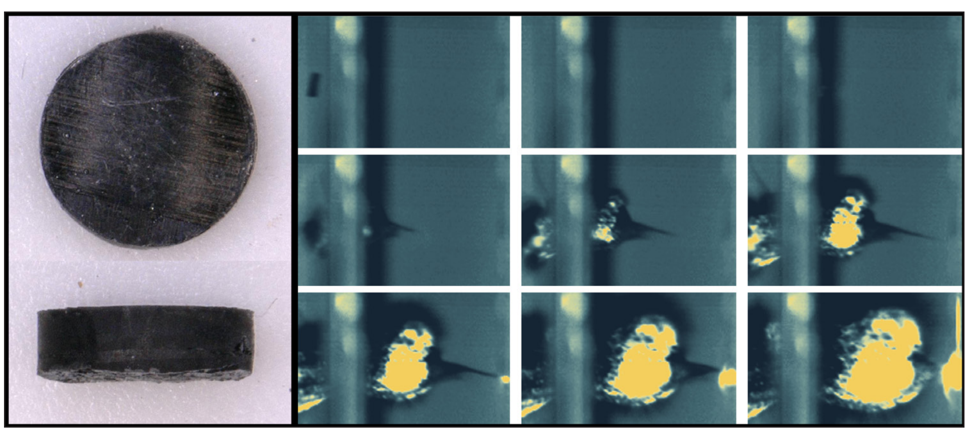

Figure 5. Images from HITF21189, which is the impact of a 0.671 mm long by 2.402 mm diameter CFRP projectile at 6.99 km/s (left). In-situ debris cloud images have been collected from just prior to the initial impact of the projectile and to interaction with the rear wall of the Whipple shield. The interframe interval shown is at 400 nanoseconds (right).

continued on page 4

Whipple Shield HVITs

continued from page 3

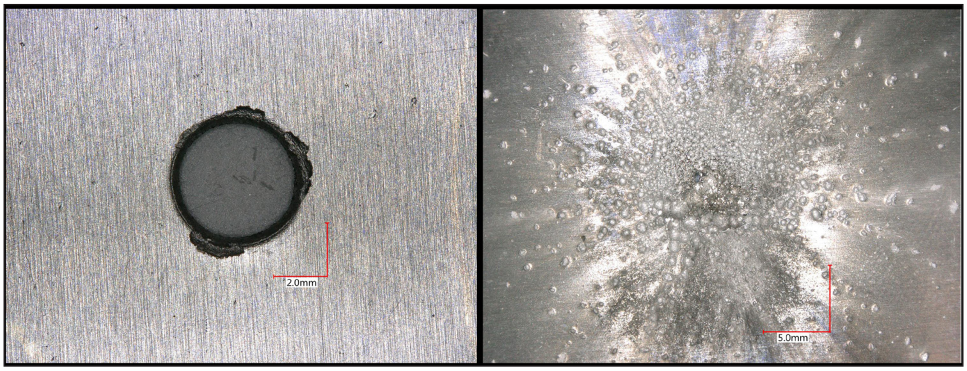

Figure 6. The results of HITF21189 are shown for the entrance hole into the shield (left) and the crater field from the debris cloud in the rear wall (right). The shield failed due to a sub millimeter diameter penetration of the rear wall.

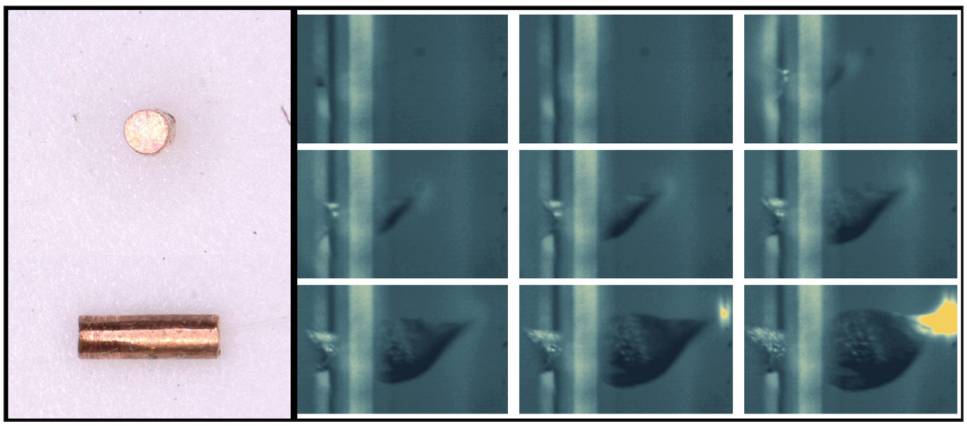

Figure 7 Images from HITF21191, which is the impact of a 1.556 mm long by 0.503 mm diameter C11000 copper projectile at 6.99 km/s (left). In-situ debris cloud images have been collected from just prior to the initial impact of the projectile and to interaction with the rear wall of the Whipple shield. The interframe interval shown is at 400 nanoseconds (right).

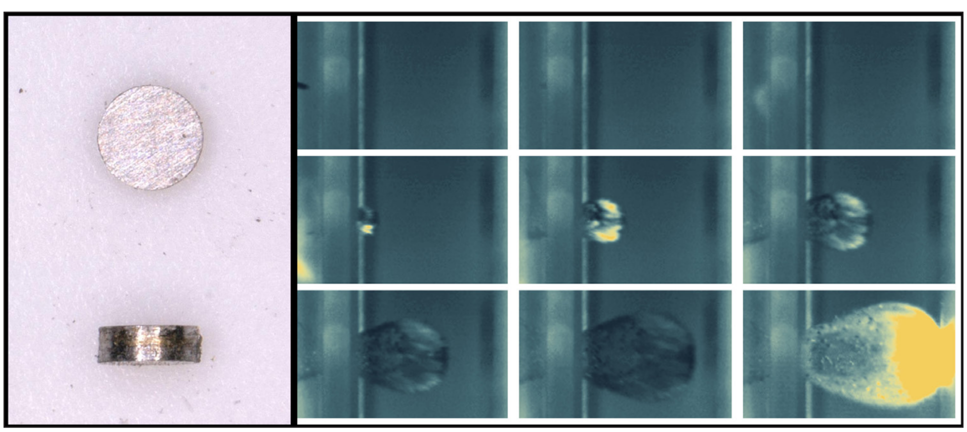

Figure 8. Images from HITF21190, which is the impact of a 0.334 mm long by 1.156 mm diameter T-304L stainless-steel projectile at 7.08 km/s (left). In-situ debris cloud images have been collected from just prior to the initial impact of the projectile and to interaction with the rear wall of the Whipple shield. The interframe interval shown is at 400 nanoseconds (right).

this projectile and impact condition.

For comparison, the low-density, "flake-like" CFRP projectile from HITF21189 is shown in Figure 5. In shot HITF21189, a 0.671 mm long by 2.402 mm diameter CFRP disk has been launched to 6.99 km/s normal to the surface of the target. During the flight of the projectile, the CFRP disk rotated to a pitch of 10.3°. The debris cloud evolution within the Whipple shield is shown at 400 ns intervals; once again, time progresses from the top right to the bottom left. For this projectile and impact condition, a jet of material preceded the debris cloud. The resultant entrance hole into the shield and the front surface of the arresting rear wall are shown in Figure 6. The shield failed for this projectile impact condition as a result of the material jet, which produced a sub-1 mm hole in the rear wall.

Having considered the geometric dependence on debris cloud for low-density projectiles, a pair of shots with high-density, metallic projectiles have been performed using the same geometric ratios to evaluate the effect of projectile material. To illustrate the findings, a comparison of the debris cloud from a copper projectile of HITF21191 that is 1.556 mm long by 0.503 mm diameter is shown in Figure 7, and the debris cloud from a stainless steel projectile from HITF21190 that is 0.334 mm long by 1.156 mm diameter is shown in Figure 8. Similar to the CFRP projectiles, both the CFRP and copper 3:1 length-to-diameter ratio projectiles produced a bulbous debris cloud; however, the copper projectile had some high-mass material that continued on to perforate the rear wall of the Whipple shield with a 3.3 mm x 3.9 mm elliptical hole. As for the 1:3 length-to-diameter ratio using the CFRP and stainless-steel projectiles, both materials produced a jet of material that advanced in front of the main debris cloud. The material jet from the stainless-steel projectile moved considerably faster than the corresponding material jet from CFRP and did not perforate the rear wall of the Whipple shield.

As can be seen from this effort, significant progress has been made in developing techniques to validate constitutive, material models for numerical simulation on low millimeter-size range, non-spherical projectile impacts. Progress has been made in the manufacturing, acceleration, and diagnoses of the orientation at the moment of impact for these non-

continued on page 5

Whipple Shield HVITs

continued from page 4

spherical projectiles. While the principal purpose of this research is to develop validation data for numerical simulation models, it is seen from this experimental effort that the geometry of the shaped projectile is a strong predictor of the nature of a debris cloud. Future work is planned to further understand the material jet formation in Whipple shields to aid in modeling this important shield and develop data for other shields of interest to robotic space flight. The combined effort of experimental validation and numerical modeling are intended to develop confidence in broad ranging ballistic-limit equations that address observations from DebriSat for use in risk assessments of spacecraft design reliability and survivability.

References

1. M. Polk, *et. al.*, "Orbital debris assessment testing in the AEDC Range G," Procedia Engineering, 103, pp. 490-498 (2015).

2. J.-C. Liou, *et. al.*, "DebriSat-A planned laboratory-based satellite impact experiment for breakup fragment characterization," International Astronautic Congress Proceedings, IAC-16. A6.2.8x35593 (2016).

3. N. Fitz-Coy, *et. al.*, "Characterization of debris from the DebriSat hypervelocity test," 66th International Astronautical Congress at Jerusalem, Israel, IAC-15-A6.2.9x30343, pp. 1-10 (2015).

4. H.M. Cowardin, *et. al.*, "Optical characterization of DebriSat fragments in support of orbital debris environment models," Advanced Maui Optical and Space Surveillance Technologies Conference proceedings, AMOS-2020.20115, (2020).

5. E.L. Christiansen, "Meteoroid/debris shielding," NASA/TP-2003-210788 (2003).

6. F.L. Whipple, "Meteorites and space travel," Astronomical Journal, 52:1161, 131 (1947).

7. J.E. Miller, *et. al.*, "Analytic ballistic performance model of Whipple shields," Procedia Engineering, 103, pp. 389-397 (2015).

8. "Comparison Data For Pultruded Shapes - CST The Composites Store, Inc.," Cstsales.Com, 2020, http://www.cstsales.com/rod_comp.html. Accessed online 2 June 2020.

9. "Ultra-Strength Lightweight Carbon Fiber Sheet," Mcmaster.Com, 020, https://www.mcmaster.com/8181K14. Accessed online 2 June 2020. ♦

PROJECT REVIEW

Analysis of NOAA-17 Breakup Fragments

J. OPIELA AND J.-C. LIOU

The U.S. National Oceanic and Atmospheric Administration (NOAA) 17 meteorological satellite (International Designator 2002-032A, Catalog number 27453) was launched in 2002 and decommissioned in 2013. The spacecraft experienced a breakup on 10 March 2021 (ODQN, Vol. 25, issue 2, p.1). The 18th Space Control Squadron of the U.S. Space Force has detected and cataloged 96 fragments associated with the breakup through 15 September 2021. Major breakups associated with spacecraft similar to NOAA-17, including NOAA-16 and two Defense Meteorological Satellite Program (DMSP) spacecraft – F11 and F13 – have been documented in the past (ODQN, Vol. 8, issue 4, p.1; ODQN, Vol. 19, issue 2, p.1; ODQN, Vol. 20, issue 1&2, p.1).

Table 1 provides a summary of the four breakups. Of these, the only breakup with a confirmed cause is DMSP F13. The spacecraft still was operational when the breakup occurred and telemetry data points

Table 1. Summary of the Four Events

Parent Object	Breakup Date	Apogee and Perigee Altitudes at Breakup	Fragments Cataloged	Fragments on Orbit
NOAA-16 (2000-055A, 26536)	25 Nov 2015	858 x 842 km	458	457
NOAA-17 (2002-032A, 27453)	10 Mar 2021	817 x 800 km	96	96
DMSP F11 (1991-082A, 21798)	15 Apr 2004	850 x 830 km	85	61
DMSP F13 (1995-015A, 23533)	3 Feb 2015	840 x 840 km	238	221

continued on page 6

Analysis of NOAA-17 Breakup

continued from page 5

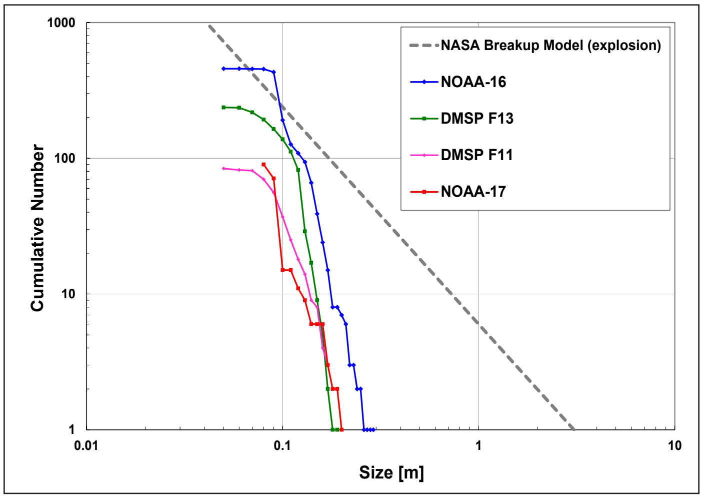

Figure 1. Cumulative size distributions of the NOAA-16, NOAA-17, DMSP F11, and DMSP F13 fragments. The gray dashed line is the power-law fragment size distribution as predicted by the NASA Standard Satellite Breakup Model for the full explosion of a spacecraft.

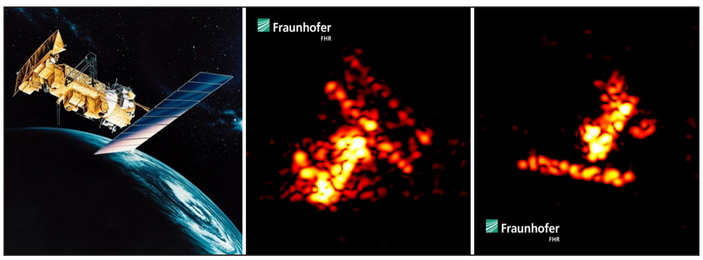

Figure 2. Artist's conception of operational NOAA-16 and two radar images taken after the breakup. (Credit: NOAA-16 radar images by Fraunhofer Society).

to a battery fault as the cause [1]. Based on the analyses described below, fragments generated from the four events have similarities, which may provide insights into the nature of the other three breakups without cause attribution.

The cumulative size distributions of the four fragment clouds are shown in Figure 1. The radar cross section of each fragment was converted to its physical size using the radar-based NASA Size Estimation Model. The distributions are comparable to one another, and most of the fragments are between 8 and 20 cm in size. For comparison, the gray dashed line is the fragment size distribution for the complete fragmentation of a spacecraft, as predicted by the NASA Standard Satellite Breakup Model [2]. The resemblance among the four fragment clouds and their difference from the gray dashed line suggest that the events were similar "localized, component-level" breakups. This is also supported by available radar images of NOAA-16 after its breakup, shown in Figure 2. Although 458 fragments have been cataloged since the breakup of NOAA-16, the post-breakup images show the spacecraft is essentially intact.

Figure 3 shows the Gabbard diagrams of the four fragment clouds approximately 3 months after the breakups. The diagrams plot the apogee altitudes and perigee altitudes against the orbital periods of the fragments at a given epoch. They provide a good visualization of the spread of the fragment clouds, which reflects the delta velocities of the fragments with respect to their parents. The cross patterns in Figure 3 are similar, especially among NOAA-16, NOAA-17, and DMSP F13 fragments, which is an indication that the nature and intensity of the breakups might be similar.

How the orbital history of a fragment was affected by the atmospheric drag perturbations can be analyzed to estimate its area-to-mass ratio (A/m). Using the NASA Orbital Debris Program Office's long-term orbit propagator PROP3D and known two-line orbital element (TLE) histories, an iterative process varies A/m to converge on the value that best predicts the actual magnitude of the semi-major axis over time. The known semi-major axis values are compared to the values as propagated from the first TLE. The derived A/m is a useful characteristic of the object and also can be used as one input to the orbit propagator to predict the object's future orbital evolution.

Figure 4 shows the A/m distributions of the four fragment clouds as a function of size. NOAA 16 and DMSP F13 fragments have two visible concentrations. The major one is between 0.2 and 0.3 m^2/kg. A secondary concentration occurs at about 0.4 to 0.6 m^2/kg. Similarly, NOAA-17 fragments share comparable concentrations. The

continued on page 7

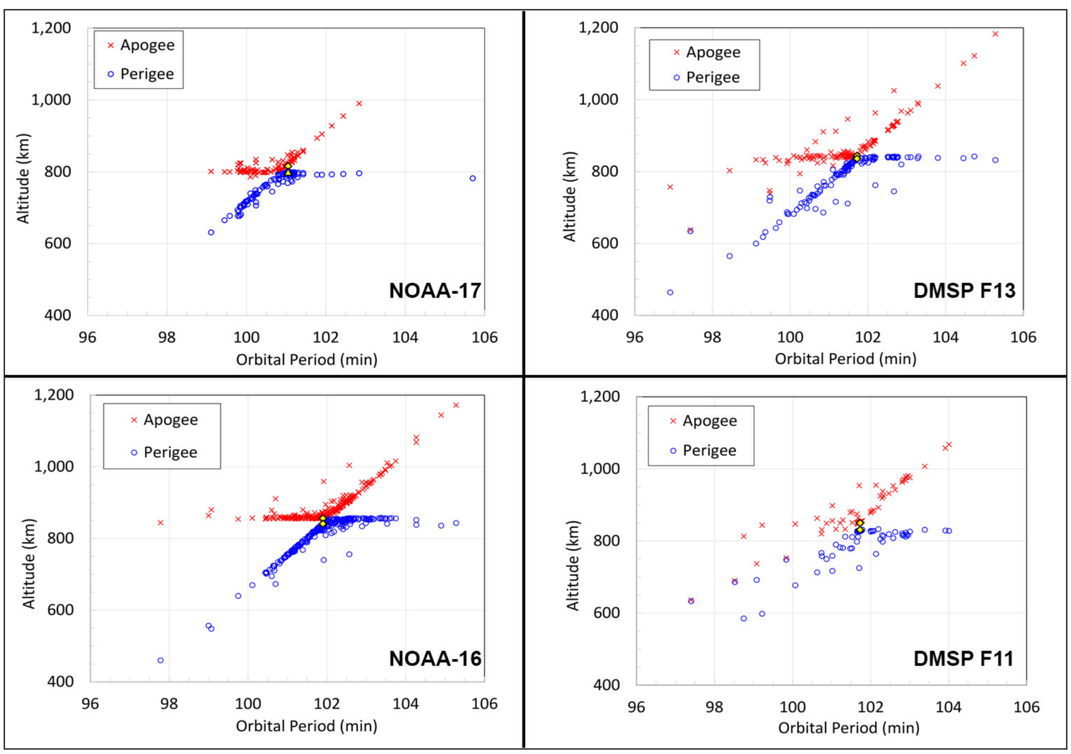

Figure 3. Gabbard diagrams of the four fragment clouds approximately 3 months after the breakup of each event. The apogee and perigee altitudes of the parent objects are indicated by the yellow-filled symbols.

Analysis of NOAA-17 Breakup

continued from page 6

histogram shown in Figure 5 provides another way to see the concentrations where all four fragment clouds have the same peak at 0.2-to-0.3 m^2/kg.

An A/m below 0.1 m^2/kg is an indication of metallic fragments. For example, using the NOAA-17 propulsion tank specifications, including the titanium material properties and the thickness of the tank wall, the A/m of titanium tank fragments are calculated to be about 0.03 m^2/kg, as indicated by the blue arrow on the Figure 4 NOAA-17 plot. Clearly, most fragments from the four breakups are not consistent with propulsion tank pieces. Fragments with A/m significantly higher than about 1 m^2/kg likely are multi-layer insulation (MLI), thermal blanket pieces, as indicated by the turned arrow on the NOAA-17 plot. Fragments with A/m between 0.1 and 1 m^2/kg, although not as heavy as metallic pieces, also are not as light as thermal blanket pieces. They are similar in nature to lightweight composite and polymer materials. The two A/m concentrations suggest that fragments from the four events share similar physical properties and that they belong to two distinct material types.

Although the number of tracked fragments from NOAA-16 and NOAA-17 differ by close to a factor of five, the fragment concentrations line up very well in size, between 9 and 10 cm, as shown by their respective plots in Figure 4. This is another indication that fragments from the two breakups are comparable in size and material type. Most likely they were generated in a similar manner from the same component(s).

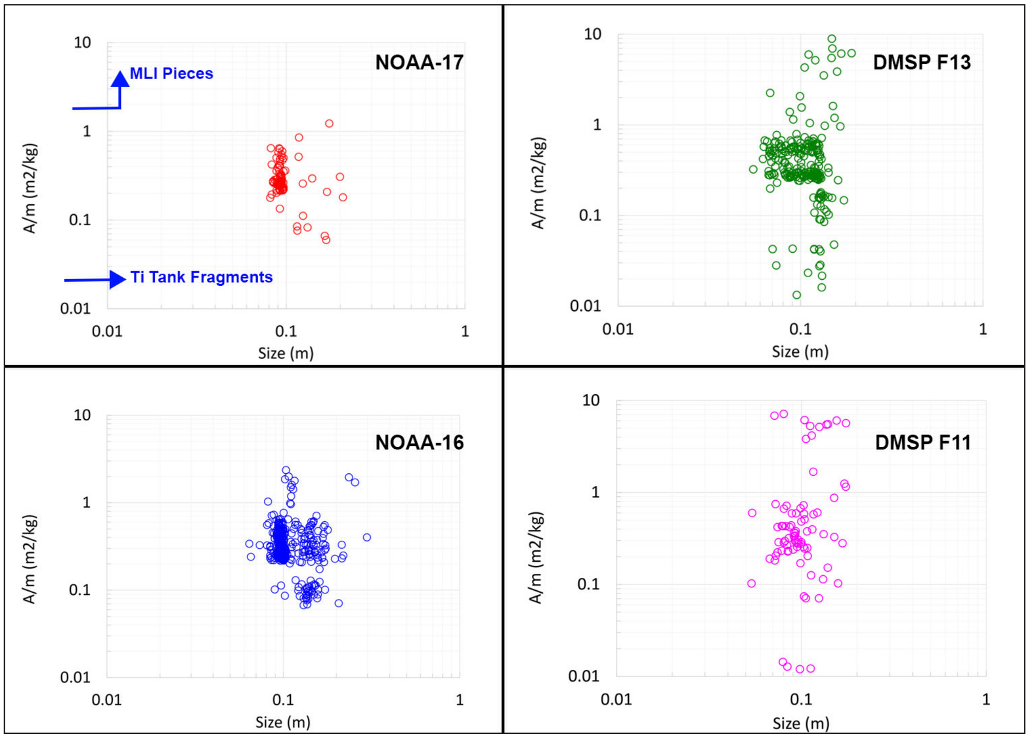

Figure 4. Area-to-mass ratio (A/m) distributions of the four fragment clouds. Most of the fragments have values between 0.1 and 1 m^2/kg, with a strong concentration at 0.2-to-0.3 m^2/kg and a secondary concentration at 0.4-to-0.6 m^2/kg. The lower blue arrow on the NOAA-17 plot indicates the A/m region for Titanium tank fragments. The upper, turned blue arrow indicates the approximate lower boundary for multi-layer insulation pieces.

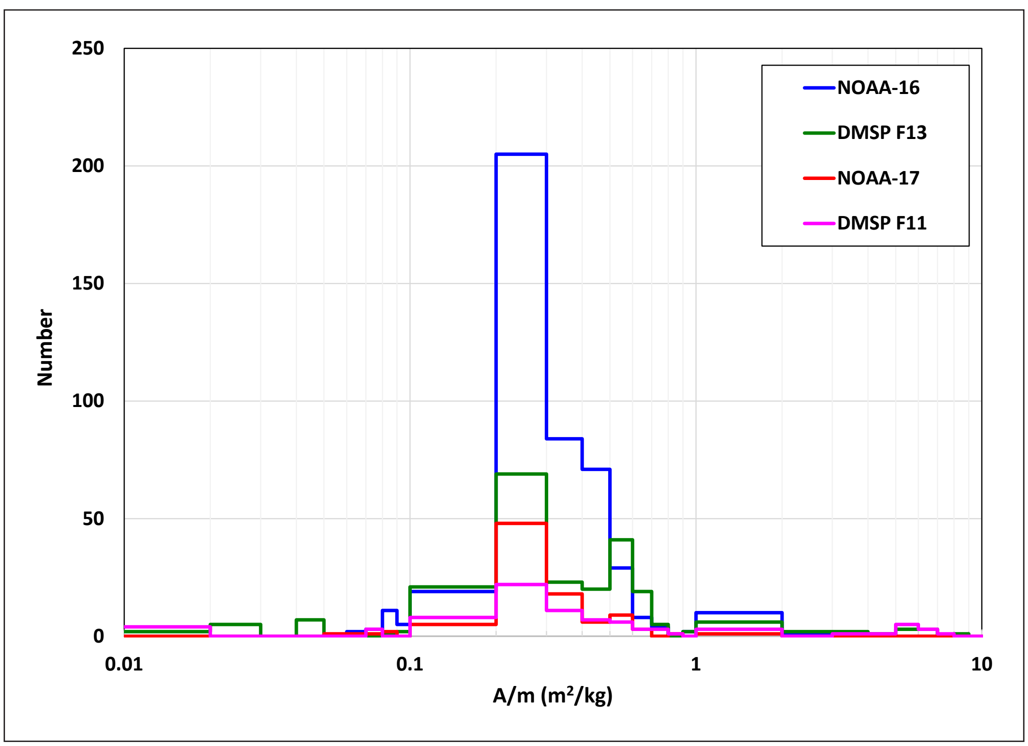

Figure 5. Area-to-mass ratio (A/m) distribution histogram. All four fragment clouds share the same peak at 0.2-to-0.3 m^2/kg.

References

1. https://www.afspc.af.mil/News/Article-Display/Article/731122/news-release-50-sw-completes-dmsp-flight-13-rupture-review/.

2. Johnson, N.L., *et al.* "NASA's new breakup model of EVOLVE 4.0," Advances in Space Research, vol 28, issue 9, pp 1377-1384, (2001). ♦

CONFERENCE AND MEETING REPORTS

The 22nd Advanced Maui Optical and Space Surveillance Technologies Conference (Hybrid) Meeting, 14-17 September 2021

The 22nd Advanced Maui Optical and Space Surveillance Technologies Conference was held in hybrid format 14-17 September 2021. This year's inaugural hybrid event hosted over 650 in-person and approximately 400 virtual participants, including representatives from 20 countries. The opening keynote speaker was Major General DeAnna M. Burt, Commander, Combined Force Space Component Command, United States (U.S.) Space Command, and Vice Commander, Space Operations Command, U.S. Space Force and Colonel Scott D. Brodeur, Director of the National Space Defense Center and Director of Operations, Joint Task Force Space Defense, U.S. Air Force, provided the second keynote address. The last keynote address was provided virtually by Carine Claeys, Special Envoy for Space/Head of the Space Task Force, European External Action Service.

This year, 4 virtual short courses and 10 additional in-person short courses were provided at the start of the conference. The Non-Resolved Object Characterization session was co-chaired by representatives of L3Harris, Odyssey Systems, and the NASA Orbital Debris Program Office (ODPO). Two papers were presented from NASA ODPO: "Characterization of the Eugene Stansbery-Meter Class Autonomous Telescope on Ascension Island" and "A New Statistical Estimate of the Radar Coverage of the Low Earth Orbit Debris Environment."

Many other papers were presented at the conference that focused on tracking, characterizing, modeling, avoiding, and removing space debris. The complete archive page of photos, videos, program and details can be viewed now at https://amostech.com/2021-amos-conference-archive/. ♦

The NASA-DOD Orbital Debris Working Group (Virtual) Meeting, 30 September 2021

The 24th annual NASA-Department of Defense (DOD) Orbital Debris Working Group (ODWG) was held virtually on 30 September 2021. This annual 1-day meeting provides the framework for cooperation and collaboration between NASA and the DOD on OD-related activities, such as measurements, modeling, mitigation, and policy development. NASA and DOD have benefited significantly from this WG and many collaborations have resulted from it. The meeting was co-chaired by the NASA Orbital Debris Program Office (ODPO); and by the Operational Assessments Division, HQ Space Operations Command, United States Space Force (USSF).

The USSF and NASA ODPO provided opening remarks, followed by a joint NASA and USSF presentation on Space Fence data collection and its contributions to the Space Surveillance Network (SSN) catalog. The Space Fence is an S-band, phased-array space surveillance radar located on Kwajalein Atoll that reached initial operational capability in March 2020. Then NASA and the USSF gave an update on conjunction assessments and potential future methods for assessing and conveying risks.

DOD personnel presented the Space Surveillance Telescope (SST) status as it proceeds toward initial operating capability. Located in Australia, the SST is anticipated to become operational in late 2022. An update on the satellite catalog transition process to nine-digit catalog numbers was provided by the USSF. Increases in launch traffic and satellite deployments, particularly large constellations, have necessitated transitioning to a nine-digit catalog sooner as the prior five-digit satellite numbers are being assigned at a higher rate in recent years. The USSF then delivered an overview on radar cross section processing updates within the SSN and its uses in sensor tasking and size estimation for conjunction assessment reporting. The final DOD presentation reviewed the recent collision between YunHai 1-02 (International Designator 2019-063A, Catalog number 44547) and SL-16 debris (International Designator 1996-051Q, Catalog number 48078). A breakup for YunHai 1-02 is covered in this issue on p. 1 and was reported in a previous issue (ODQN, vol. 25, issue 2, June 2021, p. 1).

The NASA Hypervelocity Impact Team provided the first of a series of NASA presentations with an overview of recent low Earth orbit (LEO) satellite meteoroid and orbital debris risk assessments, including a review of assessments for Landsat 9 and Joint Polar Satellite System 1 and 2 (JPSS 1 and 2). This presentation was followed by an overview of the meteoroid environment, which dominates the risk for the increasing number of missions that are being proposed and operated in cislunar and lunar space, given by the NASA Meteoroid Environment Office.

NASA ODPO then delivered an update on the development state and future enhancements that are being integrated into the next generation orbital debris engineering model, ORDEM 4.0; and a briefing on the DebriSat project and the fusion of measurements and analysis from the project into the next generation ORDEM 4.0 and NASA standard satellite breakup model. Next, an update was given on the LEO debris environment as revealed by recent measurements from the Haystack ultra-wideband satellite imaging radar and the Goldstone orbital debris radar. Closing the formal presentations for the day was ODPO's update on the Eugene Stansbery Meter Class Autonomous Telescope (ES-MCAT). The ES-MCAT reached full operational capability in September 2021. ♦

continued on page 9

REPORTS - CONT.

continued from page 8

The 11th International Association for the Advancement of Space Safety (IAASS) Conference (Virtual) 19-21 October 2021

The 11th IAASS Conference was held virtually from 15-17 October 2021, with nearly 220 members from the global space safety community. This meeting report includes highlights of the conference, with special emphasis on those presentations that may be relevant to current NASA Orbital Debris Program Office (ODPO) interests.

The conference comprised 31 technical sessions and 4 plenary sessions, covering topics from launch safety, human factors, space traffic control, space sustainability, space debris, design-for-safety, laws, regulation and standards, risk management, and reentry safety. Opening keynote addresses were given by Don Kessler, former NASA Chief Scientist for Orbital Debris, Kathy Lueders, the NASA Associate Administrator for Human Exploration and Operations Mission Directorate; Tatsushi Izumi, the Associate Director General and Senior Chief Officer of Safety and Mission Assurance at JAXA; and W. Russ DeLoach, Chief of the NASA Office of Safety and Mission Assurance. Members from the NASA ODPO presented "Design for Minimum Casualty Area – The IXPE Case," in the Reentry Safety Session, highlighting the collaborative efforts in reduced-cost design-for-minimum-risk activities between ODPO, Ball Aerospace, and NASA Marshall Space Flight Center.

The conference was followed by a virtual two-day 11th Launch and Reentry Safety Workshop, sponsored by the IAASS Launch and Reentry Safety Technical Committee and the European Space Research and Technology Centre (ESTEC). ♦

ABSTRACTS FROM THE NASA ORBITAL DEBRIS PROGRAM OFFICE

2020 NASA Aerospace Battery Workshop, 17-19 November 2020, Huntsville, Alabama, USA (Virtual)

NASA Orbital Debris Mitigation Requirements Applied to Batteries

J. OPIELA, C. OSTROM, J.-C. LIOU, AND J. BACON

This presentation reviews the current state of NASA orbital debris mitigation requirements with respect to spacecraft batteries. NASA requirements address the probability of accidental explosion during and after mission operations, and probability of human casualty resulting from reentry. Excluding post-mission explosion, these probabilities must be evaluated against quantitative limits. Reentry demisability models provide the quantitative results to assess compliance with the casualty threshold. Some projects show compliance with the explosion requirement using manufacturers' stated component or assembly reliabilities, while others cite similarity with past accepted projects. With the required threshold included in the USG ODMSP, NASA encourages the use of – and seeks – standardized methods to help quantify the probability of accidental explosion. ♦

continued on page 10

DAS 3.1 NOTICE

Attention DAS Users: DAS 3.1.2 has been updated to DAS 3.2, which requires the Windows operating system and has been extensively tested in Windows 10. Previous versions of DAS should no longer be used. NASA regulations require that a Software Usage Agreement be obtained to acquire DAS 3.2.

This software will be available in January through the NASA Software Catalog at https://software.nasa.gov/software/MSC-26690-1. Users who have already completed the software request process for earlier versions of DAS 3.x do not need to reapply for DAS 3.2. Simply go to your existing account on the NASA Software portal and download the latest installer.

An updated solar flux table (created 21 September 2021) can be downloaded for use with DAS.

ABSTRACTS - CONT.

continued from page 9

SPIE Algorithms, Technologies, and Applications for Multispectral and Hyperspectral Imaging XXVII, 12-16 April 2021 (Virtual)

Spectral Characterization of Spacecraft Materials used in Hypervelocity Impact Testing

J. REYES, H. COWARDIN, K. FULFORD, R. HOFFMANN, V. MURRAY, D. FERGUSON, E. PLIS, AND D. ENGELHART

The increasing number of successfully deployed space missions have resulted in an increased density of man-made objects positioned in orbital domains near Earth. With this steady accumulation of objects in space, it is becoming more imperative to characterize spacecraft materials, which may ultimately be contributors to the orbital debris population. In order to ascertain the potential damage from orbital debris, a laboratory hypervelocity impact test was conducted using a 56-kg modern spacecraft representative satellite (DebriSat) to simulate a catastrophic fragmentation event in low Earth orbit. In an effort to identify unique, material-specific spectroscopic markers, a select number of the spacecraft materials used to construct DebriSat were analyzed using reflectance spectroscopy as a characterization technique for assessment on material type according to optical features. Spectral measurements of DebriSat materials analyzed prior to the laboratory impact are presented in this paper. These data provide a spectral characterization baseline for modern-day spacecraft materials in their pristine conditions and are compared to each other to distinguish spectra of materials belonging to different classifications with an effort of grouping them using color index. The ongoing efforts to classify materials utilizing their reflectance spectroscopic fingerprint are discussed in this study. ♦

8th European Conference on Space Debris, 20-23 April 2021 (Virtual)

X-ray Imagery as the Record of All Data of Interest in Hypervelocity Impact Fragment Studies

J. BACON, A. ALLEN, J. FERRER, J. OPIELA, AND M. WARD

Laboratory study of hypervelocity spacecraft fragmentation has traditionally involved the collection and analysis of fragments that were caught in decelerating material surrounding the impact. This process has typically involved the disintegration of the catchment material either through chemical dissolution, or through physical excavation to recover the fragments. Due to the scale of fragmentation studies such as DebriSat and DebrisLV (each using more than 12 cubic meters of polyurethane foam to capture the fragments), these ongoing projects have used X-ray imagery to precisely locate and thus more efficiently extract fragments in the soft-catch material. Three years into the extraction process, a side study was initiated to determine additional information from the X-rays, with significant results. This study was instrumental when the project was forced to replace the X-ray system around which the extraction process had been based.

The revised process continues to map the debris for extraction. Having adapted the prior process to use alternate X-ray technology, the project is in parallel systematically addressing the limits/tolerances of what X-rays can reveal about size, shape, density, mass, velocity, energy, and deformation/damage exerted on the fragment during the deceleration in the catchment material. All these features have been optimized or have sufficient understanding to characterize the basic factors that will define a complete data set extracted solely from X-ray imagery. It is an ideal time to develop such a process, with extracted fragments providing "ground truth" against image-only data, and abundant available imagery of the same fragments under both the prior and replacement X-ray technologies, which have several fundamentally different characteristics.

This paper addresses the types and quality of hypervelocity fragmentation data that can be extracted from X-rays. It further addresses the question of whether and under what circumstances future hypervelocity experiments can use X-ray methods to largely–or to completely–avoid the extraction process in recording all appropriate results of the test. Lastly, this paper addresses lessons learned, and how future efforts might be further optimized. ♦

Pyrolysis Rate and Yield Strength Reduction in Carbon Fiber and Glass Fiber Composites Under Reentry Heating Conditions

B. GREENE AND C. OSTROM

The behavior of composite materials, specifically carbon fiber reinforced plastic (CFRP) and glass fiber reinforced plastic (GFRP), under reentry conditions poses a problem for space debris reentry risk modeling. Since these materials pyrolyze rather than melt and their different components demise at different rates, modeling their destruction to determine ground impact risk is complex. Modern spacecraft are using these materials in ever-greater quantities owing to their superior strength-to-weight characteristics, and this has required that the orbital debris community improve its understanding of how these materials demise on reentry.

The NASA Orbital Debris Program Office undertook an extensive test campaign to better understand the rate at which several types of GFRP and CFRP materials pyrolyze under reentry heating conditions and how that pyrolysis affects the ultimate strength of the material. GFRP with a polyester resin (G10/FR-4) and CFRP with epoxy, cyanate ester, vinyl ester, and phenolic resins were tested. The test campaign was carried out at the Inductively Coupled Plasma (ICP) Torch Facility

continued on page 11

ABSTRACTS - CONT.

continued from page 10

8th European Conference on Space Debris, 20-23 April 2021 (Virtual) - Cont.

Pyrolysis Rate - cont.

at the University of Texas at Austin. Because the ICP facility operates in a shirt-sleeve environment, test samples can be changed within seconds or minutes, allowing many samples to be tested in a short period. Two heat flux rates, 20 W/m^2 and 30 W/m^2, and two oxygen concentration conditions, 0% and 2% of atmospheric, were applied to all five types of material. To measure both the char rate and the effect of pyrolysis on the ultimate material strength, two types of test were carried out for each material: a char rate test on a ~10 mm thick sample of material and an *in-situ* bending stress test of a ~2 mm thick sample of material.

Measurements of the char rate showed very similar average pyrolysis front velocity in epoxy resin CFRP as in G10 at 3.6 mm/min and 3.4 mm/min, respectively. However, the total mass loss rate in the G10 was nearly double that of the CFRP at 3.8 g/min and 2.2 g/min, respectively. This result represented a slow ablation rate of carbon fibers in the CFRP at the temperatures encountered in low Earth orbit reentry and a comparatively rapid removal of the glass fibers in G10 due to melting and spallation. Pyrolysis front velocity was more significantly affected by the type of plastic than the type of fiber, with the cyanate ester CFRP samples displaying an average pyrolysis front velocity of only 1.9 mm/min.

Similarly, the effect of thermal exposure on the ultimate strength of the material depended heavily on the type of plastic and very little on the type of fiber in the material. Epoxy, vinyl ester, and polyester resins all behaved very similarly, with complete structural failure at between 400 J/g and 600 J/g of specific absorbed heat. Phenolic and cyanate ester resins, on the other hand, displayed a change in structural properties that was only barely measurable with the current apparatus even after the maximum exposure time tested.

These data are being incorporated into a numerical model of the ablation and demise of composite materials that will be used to more accurately calculate the ground casualty risk of future spacecraft. ♦

Flux Comparison of Master-8 and ORDEM 3.1 Modelled Space Debris Population

A. HORSTMANN, C. WIEDEMANN, A. MANIS, M. MATNEY, D. GATES, J. SEAGO, A. VAVRIN, AND P. ANZ-MEADOR

With ESA's Meteoroid And Space debris Terrestrial Environment Reference (MASTER-8) model and NASA's Orbital Debris Engineering Model (ORDEM) 3.1, the two premier orbital debris engineering models have been officially released. The two models come with significant enhancements and now represent state-of-the-art orbital debris modelling for their respective agencies. Both models provide the community with estimates of the space debris environment from low Earth orbit (LEO) up to at least geostationary altitude.

The MASTER population is an event-based simulation of all known events that generate debris and objects that are part of the U.S. Space Surveillance Network (SSN) catalog, which provides coverage of objects with diameters down to approximately 10 cm in LEO and 1 m in geosynchronous Earth orbit (GEO). Different models are used to simulate the artificial objects and their orbit evolution over time. These models are called "sources" since they assign an origin to each individual object and consist of fragments, solid rocket motor (SRM) remainders, sodium-potassium (NaK) droplets, paintflakes, ejecta, and multi-layer insulation (MLI) fragments. The objects from each source are characterized by having individual release mechanisms, as well as orbital distributions, material composition, size, and mass distributions. Dedicated radar and telescope observation data is used to calibrate the model for objects larger than 1 cm in LEO and larger than 10 cm in GEO. For calibrating the small-sized objects, below 1 cm, impact data from returned surfaces are analyzed. Because the >1 cm object population is dominated by fragments, the fragmentation event database was updated to include new events, as well as re-evaluate past events. Special attention was drawn to re-evaluating the Fengyun-1C anti-satellite test from 2007 and Cosmos-Iridium collision event from 2009 since these events shape the fragment population because of their severity. After 2009, the two largest fragmentations in terms of number of tracked debris are the Briz-M explosion in 2012 and the NOAA-16 explosion in 2015. In total, there are 261 confirmed fragmentations in the database up to November 2016.

The baseline population for ORDEM 3.1 is based on the U.S. SSN catalog, and observational datasets from radar, in situ, and optical sources provide a foundation from which the model populations are statistically extrapolated to smaller size regions. These regions are not well-covered by the SSN catalog yet may pose the greatest threat to operational spacecraft. The NASA Standard Satellite Breakup Model is used to generate fragments greater than 1 mm from collisions and explosions, and these fragment populations are scaled using ground-based radar data. Specific major debris-producing events, including the Fengyun-1C, Iridium 33, and Cosmos 2251 debris clouds, and unique populations, such as NaK droplets, were re-examined, modelled, and added to the ORDEM environment separately. Optical measurement data is used to model the GEO population down to 10 cm. The debris environment is propagated using NASA's LEO-to-GEO Environment Debris model, and future explosions of intact objects and collisions involving objects greater than 10 cm are assessed statistically. The environment from a few millimetres down to 10 µm is modelled using a special degradation model where small particles are generated from intact spacecraft and rocket bodies, then the populations are scaled to fit in situ cratering data from Space Shuttle returned surfaces. Fragments smaller than 10 cm are differentiated based on material density categories, i.e., high-, medium-, and low-density, to better characterize the potential debris risk posed to upper stages and spacecraft.

This paper will discuss the MASTER and ORDEM approaches for modelling populations and compare fluxes for specific orbits, including sun-synchronous, ISS-altitude, geosynchronous transfer, and GEO. In the end, a conclusion is drawn towards the importance of having multiple fundamentally different, yet validated, models to estimate the space debris population. ♦

continued on page 12

ABSTRACTS - CONT.

continued from page 11

8th European Conference on Space Debris, 20-23 April 2021 (Virtual) - Cont.

Radar Observations from the Haystack Ultrawideband Satellite Imaging Radar in 2019

J. MURRAY, T. KENNEDY, R. MILLER, AND M. MATNEY

The NASA Orbital Debris Program Office (ODPO) relies primarily on ground-based radar measurements to characterize the distribution of small debris, down to approximately 3 mm depending upon altitude and the sensor used, in low Earth orbit (LEO). Since the early 1990's, the Massachusetts Institute of Technology (MIT) Lincoln Laboratory (LL) has been collecting radar measurements for the NASA ODPO under agreements with the U.S. Department of Defense. The Haystack Ultrawideband Satellite Imaging Radar (HUSIR) is the primary ground-based radar sensor used by the ODPO and provides data on orbital debris down to an approximate size of 5.5 mm below 1000 km altitude using the NASA size estimation model (SEM). Since orbital debris of this size are a significant risk to both human and robotic missions in LEO, the sensitivity of this radar makes it a high-value sensor.

The NASA ODPO radar measurements are conducted on a continual basis for monitoring and enabling modeling of the orbital debris environment over time. HUSIR observations from 2019 are the most recent snapshot of the environment that has been measured and analyzed to date. In recent years, HUSIR measurements indicated relatively stable populations for the orbital debris objects that it is able to detect. In 2019, several interesting events happened on-orbit, including the start of large constellation deployments into LEO, as well as the Indian anti-satellite test with Microsat-R (International Designator 2019-006A, U.S. Strategic Command Space Surveillance Network catalog number 43947). Due to these events, coupled with a general increase in the number of missions and participants launching missions in recent years, continual monitoring is necessary to determine the effects of this increased activity on the orbital debris environment. This paper will explore the results of the 2019 HUSIR radar measurements, including above-average flux measurements at lower LEO altitudes and the evolution of the flux during the time of observations. ♦

Orbital Debris Mitigation and CubeSats

C. OSTROM AND J. OPIELA

The 2019 Update to the United States Government Orbital Debris Mitigation Standard Practices (ODMSP) included CubeSats for the first time as a special class of space operations. This is the first governmental-level policy document that calls for CubeSats to follow quantitative recommendations for orbital debris mitigation. While CubeSats were never exempt from such recommendations, mission designers often under assess CubeSats due to their small size and historically low level of stored energy. Qualitative assessments of debris potential are less applicable as miniaturized energy systems (propulsive and electrical) become more available and as the "CubeSat" label is applied to larger payloads. Of particular interest to the long-term evolution of the debris environment is the likelihood of accidental explosion or collision; we must also consider the risk to the human population from reentering spacecraft. We discuss the on-orbit history of CubeSats and present guidance to assist in designing for future compliance with the new standard practices. ♦

The 22nd Advanced Maui Optical and Space Surveillance Technologies Conference, 14-17 September 2021, Maui, Hawai'i

Characterization of the Eugene Stansbery-Meter Class Autonomous Telescope on Ascension Island

C. CRUZ, B. BUCKALEW, S. LEDERER, T. KENNEDY, AND H. COWARDIN

In a focused effort to meet full operational capability for NASA's Eugene Stansbery Meter Class Autonomous Telescope (ES-MCAT), a thorough system characterization analysis was completed. NASA's Orbital Debris Program Office (ODPO) utilizes ES MCAT as the primary sensor for characterizing the geosynchronous orbit (GEO) environment to acquire photometric data of small, faint debris objects in or near GEO. ES-MCAT is located on Ascension Island in the middle of the Atlantic Ocean at nearly 8° South latitude and 15° West longitude. This location provides dark skies suited for faint object observations but is also continuously subject to a harsh environment exposed to volcanic ash and salt spray.

To better assess the overall system performance of the optical instrument, a historical assessment of the system's performance was conducted. This analysis investigated all systematic and optical operational data to determine the overall performance parameters for ES-MCAT.

A complete optical system throughput calculation was performed to determine the optimal filter for observing orbital debris in GEO orbits. The responses of each optical component to the solar spectrum, with atmospheric absorption, were multiplied and integrated to give ES-MCAT's total system response for various filters. With the highest flux values, the Sloan Digital Sky Survey (SDSS) r' and g' were determined to be the optimal filters for ES-MCAT observations. Further analysis with known GEO debris objects enabled the selection of the r' filter for characterization of the GEO debris population.

A detailed overview of the optical system throughput, data reduction, photometric and astrometric data, and other system characteristics that define ES-MCAT will be discussed in the subsequent paper. ♦

continued on page 13

ABSTRACTS - CONT.

continued from page 12

The 22nd AMOS Conference, 14-17 September 2021, Maui, Hawai'i - Cont.

A New Statistical Estimate of the Radar Coverage of the Low Earth Orbit Debris Environment

C. OSTROM AND T. KENNEDY

For over three decades, the NASA Orbital Debris Program Office (ODPO) has used the Goldstone Orbital Debris Radar, Haystack Ultrawideband Satellite Imaging Radar (HUSIR), and Haystack Auxiliary (HAX) radar assets to collect data on the low Earth orbit (LEO) debris environment. Each radar, with its unique beamwidth, altitude and inclination coverage, and limiting size threshold, operates in a beam park mode to statistically sample the orbital debris population in LEO. Provided that these assets are shared with other users, the orbital debris data collection is not continuous; rather, intermittent data collects are acquired and sent to the NASA ODPO. To understand the sampling process conducted by each radar over time and any related observational biases, a Statistical Confirmation of Radar Uniformity or Bias (SCRUB) code has been implemented to model the coverage of these assets for informing future operations, as well as usage of the data collected from these ground-based sensors. For this analysis, Right Ascension of the Ascending Node (RAAN) is used as a metric to measure statistical coverage. A complete survey of the LEO environment is understood to be measurements that sufficiently sample all values of RAAN for each altitude-inclination pair visible from the radar asset. Regions of incompleteness or statistical bias can help inform future observation campaigns.

The SCRUB tool evaluates the coverage of the LEO environment, not by examining individual objects that may pass through a sensor's field of view (FOV), but by determining which orbit planes pass through the FOV. Once a pointing geometry for a radar site, observation time, and range extent are configured by the user, SCRUB computes the inclinations and altitudes that are visible by the sensor. For each inclination-altitude pair, there is a distinct pair of possible RAAN values, corresponding to the ascending and descending orbit passing through that point in the sensor cone. Repeating this process for all points in the beam, and for multiple time periods during an observation window, creates a matrix of all inclination-altitude-RAAN combinations that are visible during a sensor run. This process can then be repeated for all observations within a year (for an annual survey), propagating all the RAAN values to a common epoch, and combining the observations to assemble a full estimate of the RAAN coverage of the LEO environment. This RAAN coverage can then be analyzed for uniformity of sampling, within a certain inclination-altitude pair, or between larger regions of the space environment.

This paper provides a general overview of the radar assets utilized by ODPO, typical analysis data products assuming circular orbits, and an in-depth discussion on the algorithms that feed between modeling and measurement operations. Following the description of the algorithm, estimates of coverage using HUSIR radar data collected from multiple years are developed and compared to a 24/7 sampling scheme. ♦

11th International Association for the Advancement of Space Safety (IAASS) Conference, 19-21 October 2021, Rotterdam, The Netherlands (Virtual)

Design for Minimum Casualty Area – The IXPE Case

C. OSTROM, J. MARICHALAR, B. GREENE, W. DEININGER, A. WALDEN, J. BACON, AND C. SANCHEZ

The Imaging X-Ray Polarimetry Explorer (IXPE) is a new international space observatory in NASA's Small Explorer program, designed in a collaboration between the Italian Space Agency and NASA's Marshall Space Flight Center, and built by Ball Aerospace. IXPE has an expected launch in May 2021, to a 600-km altitude equatorial orbit. IXPE is an astrophysics mission using three telescope assemblies to measure the polarization of cosmic X-rays. Each assembly is composed of a mirror module assembly (MMA) with 24 nested nickel-cobalt cylinders and a unique, polarization-sensitive, gas pixel detector (GPD) within the detector unit (DU). As a NASA mission, IXPE must adhere to the orbital debris mitigation requirements specified in NASA Standard 8719.14 [1]; in the present work, we will only discuss reentry human casualty risk.

As initially designed, the IXPE observatory exceeded NASA's casualty risk threshold. IXPE does not include a propulsion system to perform a controlled reentry at the end of mission to mitigate the ground casualty risk. To reduce the risk from the uncontrolled reentry of this observatory, the IXPE design team worked with the NASA Orbital Debris Program Office to reduce the debris casualty area through design-for-demise and containment methods. The flight design of IXPE is now compliant with the ground casualty risk requirement at a casualty probability of 1:13,100 compared to a casualty requirement of better than 1:10,000. ♦

SATELLITE BOX SCORE

(as of 4 November 2021, cataloged by the U.S. SPACE SURVEILLANCE NETWORK)

Country/ Organization	Spacecraft*	Spent Rocket Bodies & Other Cataloged Debris	Total
CHINA	500	3857	4357
CIS	1553	5748	7301
ESA	93	60	153
FRANCE	76	514	590
INDIA	102	116	218
JAPAN	200	120	320
UK	411	2	413
USA	3878	5177	9055
OTHER	1011	104	1115
TOTAL	7824	15698	23522

* *active and defunct*

Visit the NASA
Orbital Debris Program Office Website

www.orbitaldebris.jsc.nasa.gov

Technical Editor
Heather Cowardin, Ph.D.

Managing Editor
Rossina Miller

Correspondence can be sent to:

J.D. Harrington
j.d.harrington@nasa.gov

or to:
Nilufar Ramji
nilufar.ramji@nasa.gov

INTERNATIONAL SPACE MISSIONS

01 June 2021 – 31 August 2021

Intl.* Designator	Spacecraft	Country/ Organization	Perigee Alt. (KM)	Apogee Alt. (KM)	Incli. (DEG)	Addnl. SC	Earth Orbital R/B	Other Cat. Debris
1998-067	ISS dispensed payloads	Various	418	422	51.7	4	0	1
2021-047A	FENGYUN 4B	PRC	35777	35798	0.2	0	1	0
2021-048A	DRAGON CRS-22	US	202	318	51.6	0	0	2
2021-049A	XM-8	US	35780	35794	0.1	0	1	0
2021-050A	OBJECT A	PRC	485	501	97.5	0	0	0
2021-050B	OBJECT B	PRC	484	503	97.5			
2021-050C	OBJECT C	PRC	484	502	97.5			
2021-050D	OBJECT D	PRC	485	505	97.5			
2021-051A	ODYSSEY	US	397	446	97.5	0	1	0
2021-052A	USA 316	US	584	606	55.0	0	1	0
2021-052B	USA 317	US	589	602	55.0			
2021-052C	USA 318	US	589	604	55.0			
2021-053A	SZ-12	PRC	384	390	41.6	0	1	5
2021-053C	SZ-12 MODULE	PRC	381	390	41.6			
2021-054A	NAVSTAR 81 (USA 319)	US	20174	20191	55.1	0	0	0
2021-055A	YAOGAN-30 AA	PRC	594	602	35.0	0	1	0
2021-055B	YAOGAN-30 AB	PRC	594	602	35.0			
2021-055D	YAOGAN-30 AC	PRC	594	602	35.0			
2021-055E	TIANQI-14	PRC	588	599	35.0			
2021-056A	COSMOS 2550	CIS	458	470	67.1	0	1	0
2021-057A	PROGRESS MS-17	CIS	417	423	51.7	0	1	0
2021-058B	STORK-5 (MARTA)	POL	484	526	60.7	6	0	1
2021-059A	STARLINK-3003	US	512	524	97.5	85	0	0
2021-060A	ONEWEB-0249	UK	1197	1199	87.9	35	0	0
2021-061A	OBJECT A	PRC	530	545	97.5	0	0	0
2021-061B	OBJECT B	PRC	527	543	97.5			
2021-061C	OBJECT C	PRC	528	544	97.5			
2021-061D	OBJECT D	PRC	528	544	97.5			
2021-061E	OBJECT E	PRC	528	544	97.5			
2021-062A	FENGYUN 3E	PRC	825	827	98.7	0	1	3
2021-063A	TIANLIAN 1-O5	PRC	35773	35803	2.7	0	1	0
2021-064A	NINGXIA-1 6	PRC	861	871	45.0	0	1	0
2021-064B	NINGXIA-1 7	PRC	861	871	45.0			
2021-064C	NINGXIA-1 8	PRC	861	871	45.0			
2021-064D	NINGXIA-1 9	PRC	861	871	45.0			
2021-064E	NINGXIA-1 10	PRC	861	871	45.0			
2021-065A	YAOGAN-30 AD	PRC	593	603	35.0	0	1	0
2021-065B	TIANQI-15	PRC	588	599	35.0			
2021-065C	YAOGAN-30 AE	PRC	597	599	35.0			
2021-065D	YAOGAN-30 AF	PRC	594	601	35.0			
2021-066A	ISS (NAUKA)	CIS	DOCKED TO ISS			0	1	0
2021-067A	TIANHUI 1-04	PRC	494	496	97.5	0	0	0
2021-068A	MONOLITH	US	598	610	37.0	0	2	0
2021-069A	STARONE D2	BRAZ	35776	35797	0.0	0	1	1
2021-069B	EUTELSAT QUANTUM	EUTE	35775	35798	0.1			
2021-070A	KL-BETA A	GER	898	909	89.0	0	1	0
2021-070B	KL-BETA B	GER	898	909	89.0			
2021-071A	CHINASAT 2E	PRC	35778	35796	0.1	0	1	0
2021-072A	CYGNUS NG-16	US	417	423	51.7	0	1	0
2021-073A	BRO-4	FR	521	562	97.6	0	0	0
2021-073B	RADCUBE	HUN	525	563	97.6			
2021-073C	SUNSTORM	FIN	525	563	97.6			
2021-073D	LEDSAT	IT	525	564	97.6			
2021-073E	PNEO4	FR	623	625	97.9			
2021-074A	TIANHUI 2-02A	PRC	514	517	97.5	0	1	1
2021-074B	TIANHUI 2-02B	PRC	514	517	97.5			
2021-075A	ONEWEB-0285	UK	598	625	87.5	33	0	0
2021-076A	RSW-01	PRC	1086	1112	86.4	0	0	0
2021-076B	PAYLOAD B	PRC	848	880	86.4			
2021-076C	RSW-02	PRC	1084	1115	86.4			
2021-077A	TJS-7	PRC	35778	35794	0.9	0	1	0
2021-078A	DRAGON CRS-23	US	417	423	51.7	0	0	1

* *Intl. = International; SC = Spacecraft; Alt. = Altitude; Incli. = Inclination; Addnl. = Additional; R/B = Rocket Bodies; Cat. = Cataloged*

Notes:

1. Orbital elements are as of data cut-off date 3 July

2. Additional spacecraft on a single launch may have different orbital elements.

National Aeronautics and Space Administration
Lyndon B. Johnson Space Center
2101 NASA Parkway
Houston, TX 77058

www.nasa.gov
https://orbitaldebris.jsc.nasa.gov/

The NASA Orbital Debris Photo Gallery has added high resolution, computer-generated images of objects in Earth orbit that are currently being tracked. They may be downloaded. Full instructions are at the webpage:

https://orbitaldebris.jsc.nasa.gov/photo-gallery/